Discrete Alfvén eigenmodes in the CFETR steady-state scenario

Yuan-Dan Lan(兰源丹)[†], Shuang-Hui Hu(胡双辉)[‡], Si-Jie Ouyang(欧阳思杰), Wan-Po Zhu(朱万坡), and Xuan-Ge Huang(黄旋格)

College of Physics, Guizhou University, Guiyang 550025, *China*

(Received 21 August 2022; revised manuscript received 29 October 2022; accepted manuscript online 17 November 2022)

The stability features of discrete Alfvén eigenmodes (αTAEs) trapped by α-induced potential wells are explored in the China Fusion Engineering Test Reactor (CFETR) advanced steady-state operation environment, where α denotes a measure of the pressure gradient. For the reversed magnetic shear (RS) H-mode scenario with an enhanced internal transport barrier (ITB), the αTAEs are trapped in the electron cyclotron (EC) power deposition region and the effects of different pedestals on αTAEs are analyzed. For the negative off-axis magnetic shear scenario, the αTAEs are discussed, and the effect of different magnetic shears on the αTAEs is presented. Finally, the effects of beam energies and pitch-angle distributions on αTAE stability are also presented.

Keywords: Alfvén wave, energetic particles, plasma instability

PACS: 52.35.Bj, 52.50.Gj, 96.50.Vg, 52.65.–y **DOI:** 10.1088/1674-1056/aca397

1. Introduction

The China Fusion Engineering Test Reactor (CFETR) is the next device for the realization of fusion energy in China,[1,2] which is proposed to fill the gap between ITER[3] and DEMO.[4] The Alfvén wave has played a crucial part in the magnetic confinement fusion field. Various Alfvén eigenmodes (AEs)[5–8] have been explored, such as the toroidicity-induced Alfvén eigenmode (TAE),[9–11] the reversed shear Alfvén eigenmode (RSAE),[12–14] and the α-induced toroidal Alfvén eigenmode (αTAE).[15,16] Here, $\alpha = -q^2 R \mathrm{d}\beta/\mathrm{d}r$, q is the safety factor, R and r are the major and minor radii in tokamaks, respectively, and β is the ratio between thermal and magnetic pressures. The αTAEs are magnetohydrodynamic (MHD) eigenmodes trapped in the α-induced potential wells along the magnetic field line.[15] The αTAEs exist independently of the toroidal Alfvén frequency gap. The usual TAEs exist in the toroidal Alfvén frequency gap.[15] The stability of the αTAE is one important issue in CFETR. In recent years, theoretical study of the αTAE has been carried out in specific operation scenarios on actual tokamaks.[17–22] Energetic particles produced in the auxiliary heating or the fusion reaction can drive Alfvén instabilities.[23] The Alfvén instabilities could potentially affect the fusion device confinement. Based on the ITER design, the reversed magnetic shear (RS) scenario of CFETR achieves better confinement by modifying radio-frequency wave launch parameters.[24] In the ITER scenario of Ref. [25], the αTAEs are trapped in the electron cyclotron (EC) power deposition region and other regions. The αTAEs have different distribution features in the CFETR RS scenario.

There are two typical scenarios of CFETR: the RS H-mode scenario with an enhanced internal transport barrier (ITB)[24] and the local negative shear at large minor radius (negative off-axis magnetic shear) scenario.[26] Both the fusion performance target ($P_{\mathrm{fusion}} > 1000$ MW, $Q_{\mathrm{plasma}} > 10$) and the avoidance of global ideal MHD instabilities can be reached simultaneously in the RS H-mode scenario with enhanced ITB for CFETR.[24] The negative off-axis magnetic shear scenario appears to be beneficial for stabilization of turbulence and increasing the no-wall limit.[26] In this paper, the motivation is to study the instability of αTAEs in the two scenarios. For the RS H-mode scenario with an enhanced ITB, we explore the αTAE stability under the different EC power conditions, and the effects of different pedestals on αTAEs are analyzed. In the negative off-axis magnetic shear scenario, we discuss the stability of the αTAE, and the effects of negative magnetic shears on αTAEs are studied.

This paper is organized as follows. The theoretical models for αTAEs are introduced in Section 2. Section 3 investigates the αTAEs in the RS H-mode scenario with the enhanced ITB. Section 4 explores the αTAEs in the different pedestal cases. In Section 5, the αTAEs in the negative off-axis shear scenario are also studied. Finally, the conclusions are given in Section 6.

2. Theoretical model

When axisymmetric toroidal plasma with a large aspect ratio (i.e., $\varepsilon = a/R \ll 1$) and shifted circular magnetic surfaces are considered, we adopt high-n (n is the toroidal mode number) ballooning mode formalism[27] and the (s, α) model equilibrium[28] to study the instability of discrete Alfvén eigenmodes (the magnetic shear $s = r(\mathrm{d}q/\mathrm{d}r)/q$). The plasma is considered to consist of a core (C) and an energetic (E)

[†]Corresponding author. E-mail: lyuandan@163.com
[‡]Corresponding author. E-mail: shhu@gzu.edu.cn

© 2023 Chinese Physical Society and IOP Publishing Ltd

component with formal ordering.[29,30] The core component considered as the ideal MHD fluid supports the Alfvén eigenmode, while the kinetic instability drive is provided by the energetic component. The shear Alfvén-ballooning modes are governed by the following vorticity equation:[29,30]

$$(1+2\varepsilon_0\cos\theta)\frac{\partial^2\delta\psi}{\omega_{\rm A0}^2\partial t^2} = \frac{\partial^2\delta\psi}{\partial\theta^2} - (V+V_\rho)\,\delta\psi - \frac{q^2R^2}{f^{1/2}}\frac{4\pi q_{\rm E}}{c^2}\langle\Omega_{\rm d}J_0\delta G\rangle, \quad (1)$$

where $\omega_{\rm A0}=v_{\rm A0}/(qR)$ is the Alfvén frequency, $v_{\rm A0}$ is the Alfvén speed, and $\varepsilon_0=2(\varepsilon+{\rm d}\Delta/{\rm d}r)$ with Δ being the Shafranov shift. Here, $V=(s-\alpha\cos\theta)^2/f^2-\alpha\cos\theta/f$ is the potential $V(\theta)$, where $-\infty<\theta<\infty$ is the extended poloidal angle coordinate along the magnetic field,. Meanwhile, $f=1+[s(\theta-\theta_{\rm k})-\alpha\sin\theta]^2$, $\alpha=\alpha_{\rm C}+\alpha_{\rm E}$, $\alpha=-q^2R{\rm d}\beta/{\rm d}r$, $\theta_{\rm k}=k_{\rm r}/(n{\rm d}q/{\rm d}r)$ where $k_{\rm r}$ is the WKB wave number of the radial envelope, and $V_\rho=-\alpha_{\rm E}g/f-\left(q^2R^2/f\right)4\pi q_{\rm E}^2/\left(m_{\rm E}c^2\right)\langle\hat{\Omega}_*F_0J_0(\Omega_{\rm k}J_0-\Omega_\rho J_2)\rangle$ is the finite Larmor-radius correction to V because of the energetic particles. Here, $q_{\rm E}$ and $m_{\rm E}$ are the charge and mass of energetic particles, respectively. Meanwhile, $g=\cos\theta+[s(\theta-\theta_{\rm k})-\alpha\sin\theta]\sin\theta$, $\hat{\Omega}_*F_0=-(\partial F_0/\partial r)/\omega_{\rm c}$, $\langle\cdots\rangle=2\pi\sum_{\hat{\sigma}}\int_0^\infty{\rm d}E\int_0^{E/B}{\rm d}\mu\left(B/|v_\parallel|\right)(\cdots)$, where $\hat{\sigma}$ is the sign of the parallel velocity, $E=(v_\perp^2+v_\parallel^2)/2$, $\mu=v_\perp^2/(2B)$, and $J_0=J_0(\lambda)$ and $J_2=J_2(\lambda)$ are the Bessel functions with

$$\lambda=\sqrt{f}k_\theta v_\perp/\omega_{\rm c},\quad \omega_{\rm c}=q_{\rm E}B/(m_{\rm E}c),$$
$$\omega_{\rm p}=-\frac{4\pi\mu}{B}\frac{\boldsymbol{k}\times\boldsymbol{e}_\parallel\cdot\nabla P_{\rm C}}{\omega_{\rm c}}=-\frac{\alpha_{\rm C}}{q^2}\frac{k_\theta}{R\omega_{\rm c}}\frac{v_\perp^2}{4}=k_\theta\Omega_{\rm p},$$
$$\omega_\kappa=k_\theta g\left(\mu B+v_\parallel^2\right)/(R\omega_{\rm c})=k_\theta\Omega_{\rm k},$$
$$\omega_{\rm d}=\omega_{\rm k}+\omega_{\rm p}=k_\theta\Omega_{\rm d},\quad k_\theta=nq/r,$$

where k_θ is the poloidal mode. In Eq. (1), the left-hand side is the inertial term and the right-hand side consists of the field-line bending (first), the ballooning/interchange driving (second), and the kinetic compression (third) terms. The causality constraint also corresponds, in the ideal MHD stable domain, to the outgoing wave boundary conditions and, thus, makes it possible to describe tunneling leakage of the wave energy, as detailed in Ref. [15].

The Alfvén instabilities are driven by the kinetic compression term in Eq. (1) in which the energetic component, described by the nonadiabatic response function δG, is governed by the linear gyrokinetic equation[29,30]

$$\left(\frac{\partial}{\partial t}+\frac{v_\parallel}{qR}\frac{\partial}{\partial\theta}+{\rm i}\omega_{\rm d}\right)\delta G = {\rm i}\frac{q_{\rm E}}{m_{\rm E}}\frac{QF_0}{f^{1/2}}\left(\Omega_{\rm k}J_0-\Omega_\rho J_2\right)\delta\psi, \quad (2)$$

where $QF_0={\rm i}\left(\partial/\partial t\right)\partial F_0/\partial E+\hat{\omega}_*F_0$. The bounce and precessional motions of the trapped particles are represented by the left-hand side, together with the free energy source in both configuration and velocity spaces on the right-hand side. The time-centered numerical scheme is used to solve the coupled Eqs. (1) and (2). When the vorticity equation is solved by a finite difference algorithm, the gyrokinetic equation is simulated using the perturbation distribution function method (δf method)[31] with an equilibrium marker loading.[32] The particle-in-cell (PIC) method[33] can achieve coupling between the discrete grid representation and the continuous particle coordinates. Each marker is loaded with specified E and μ, which satisfies the given equilibrium distribution. The total marker number is conserved. The energy and the momentum are conserved in the numerical scheme, because the E and μ assigned to each marker remain unchanged during the marker motion. The δG is defined by its weighing function on the markers, whose phase-space trajectories represent the unperturbed characteristics governed by the gyrokinetic equation. The markers are loaded to carry out a Maxwellian distribution $F_0=n_{\rm E0}/(2\pi T_{\rm E0})^{3/2}\,{\rm e}^{-E/T_{\rm E0}}$, where $n_{\rm E0}$ and $T_{\rm E0}$ are, respectively, the density and temperature of energetic particles at $\theta=0$ with their radial scales characterized by both the $\eta_{\rm E}={\rm d}\ln T_{\rm E0}/{\rm d}\ln n_{\rm E0}$ and the pressure scale length $L_{\rm P0}$. It is qualitatively similar in the Maxwellian distribution and slowing down.[34] The αTAE instability is carried out in the Maxwellian distribution. The differences between two distributions are discussed in Refs. [34,35].

In this paper, the instability features of αTAEs are demonstrated using the gyrokinetic-MHD hybrid model. The kinetic excitations of αTAEs are demonstrated for a given k_θ, in the approximation of transnational invariance, with trapped energetic particles.[34,36]

3. αTAES in RS H-mode scenario with enhanced ITB

The heating and current drive (H&CD) consist of neutral beam injection (NBI) and an electron cyclotron wave (ECW).[24] The ECW power is 75 MW.[24] In this scenario, we explore the stability properties and kinetic excitation of αTAEs.

3.1. The stability feature of αTAE

Based on the plasma profiles quoted from Ref. [24], we obtain the distributions of s, α and αTAE (1,0) mode versus the normalized radius ρ ($\rho=r/a$) in Figs. 1(a) and 1(b). The EC power deposits in the range of $\rho\approx0.38$–0.6 where the pressure gradient is steep, as shown in Fig. 1(c). The αTAEs are trapped in the EC power deposition region, as shown in Fig. 1(b). For the $\rho\approx0.2$–0.38, there is a pressure gradient and the $|s|$ is relatively small. There are αTAEs trapped in the $\rho\approx0.2$–0.38.

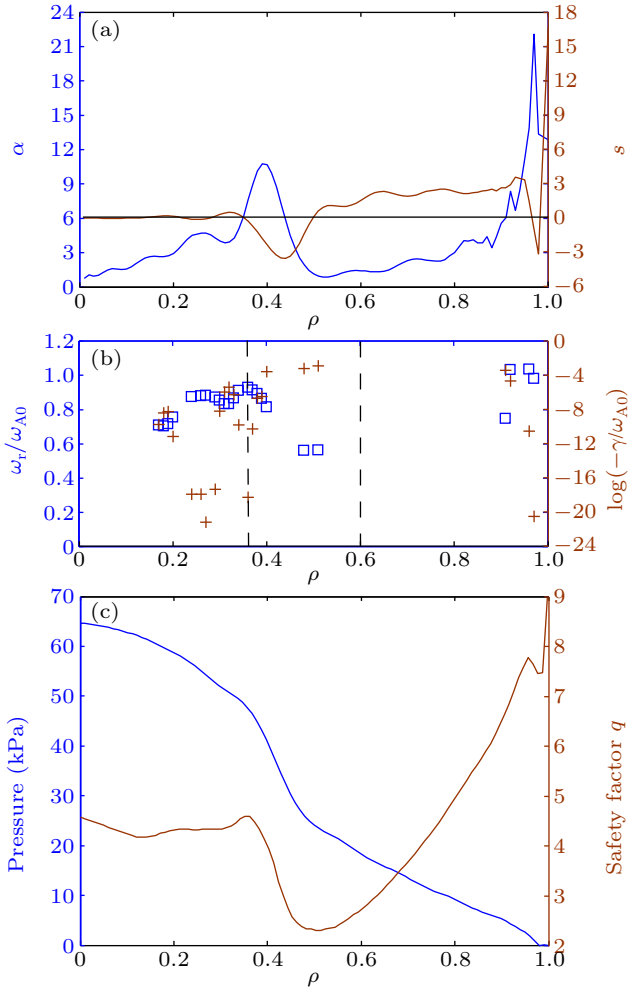


Fig. 1. (a) The parameters of (s, α), (b) the distribution of αTAE (1,0) mode and (c) the pressure profile[24] and the q profile[24] in the RS H-mode scenario with enhanced ITB; the squares (□) and crosses (+) respectively describe the real frequencies ω_r/ω_{A0} and the parameter relating to imaginary frequencies $\log(-\gamma/\omega_{A0})$.

In the negative magnetic shear region, the relatively small $|s|$ and the relatively large α can easily form potentials to trap the αTAEs. Therefore, we select the local parameter $\rho = 0.24$ (i.e., $s = -0.14$ and $\alpha = 4.52$) to obtain multiple branches of αTAEs trapped in the potential well to clearly clarify the eigenmode structure feature. The potential well structures are plotted in Fig. 2(a), where the each jth well can have different lth eigenstates, denoted by αTAE (j,l). The potential well is represented by the j (j = 1,2,3,4,5); the energy level is represented by the l (l = 0,1,2). For example, for the (1,0) mode, the "l" represents the dominant potential well ($j = 1$) and the "0" represents the ground state ($l = 0$). The eigenmode structures of αTAE (1,0), (1,1), (1,2), and (2,0) are shown in Figs. 2(b)–2(e), respectively. The corresponding real frequency is $\omega_r/\omega_{A0} = 0.88$, 1.00, 1.83, and 0.82, respectively. In the same j but different l, the αTAE with larger l corresponds to a higher real frequency (such as (1,0) mode, (1,1) mode, and (1,2) mode). For the same l but different j, the αTAE with larger j corresponds to a lower real frequency (such as (1,0) mode and (2,0) mode).

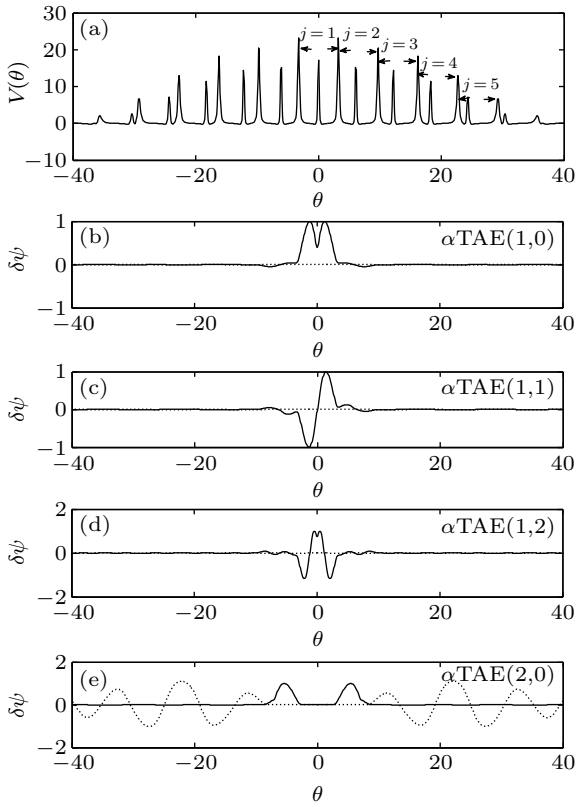


Fig. 2. (a) Potential V. (b) $\delta\psi(1,0)$, (c) $\delta\psi(1,1)$, (d) $\delta\psi(1,2)$, and (e) $\delta\psi(2,0)$ versus θ for $s = -0.14$, $\alpha = 4.52$ in MHD. Real and imaginary $\delta\psi$ are plotted using solid and dashed lines, respectively. Here, $j = 1(\theta \in (-10/3, 10/3))$, $j = 2(\theta \in (10/3, 30/3))$, $j = 3(\theta \in (30/3, 50/3))$, and so on. The potential well on the left side of $\theta = 0$ is the result of the axisymmetric right-side well.

3.2. The kinetic excitation of αTAE

The energetic particles are accompanied by the pitch angle scattering in the process of slowing down.[37] The pitch angle is the parameter between the particle motion direction and the parallel magnetic field. The θ_b means the angle at which the particle is bounced. The θ_b indicates the pitch-angle parameter. The energetic particles are injected at different angles. With the changes in v_E/v_{A0}, the formant position may shift. Therefore, we explore the αTAE instability in the different pitch-angle distributions. The different pitch-angle distributions are as follows: [10°, 70°], [70°, 110°].

We still choose the physical parameter at $\rho = 0.24$. In addition to s and α, the remaining parameters are $q = 4.34$, $k_\theta \rho_{A0} = 0.4$, $\beta_{E0} = 0.07$ (β_{E0} is the ratio between the energetic particle and magnetic pressures), $\theta_k = 0$, $\varepsilon = 0.2$, $\varepsilon_0 = 0.2$, $L_{P0} = -0.1$, and $\eta_E = 1.0$. The interval of v_E/v_{A0} is in [0.2, 1.0].

In the range of [10°, 70°], the excitation of αTAEs versus v_E/v_{A0} is plotted in Fig. 3(a). As the v_E/v_{A0} increases, the four eigenmodes (5,0), (5,3), (3,3), and (1,4) are excited. Figures 3(c)–3(f) show the four eigenmode structures with maximal growth rates at $v_E/v_{A0} = 0.20$, 0.34, 0.55, and 0.73, respectively. The real frequencies of the four modes are $\omega_r/\omega_{A0} = 0.38$, 1.03, 2.12, and 2.62, respectively. Their

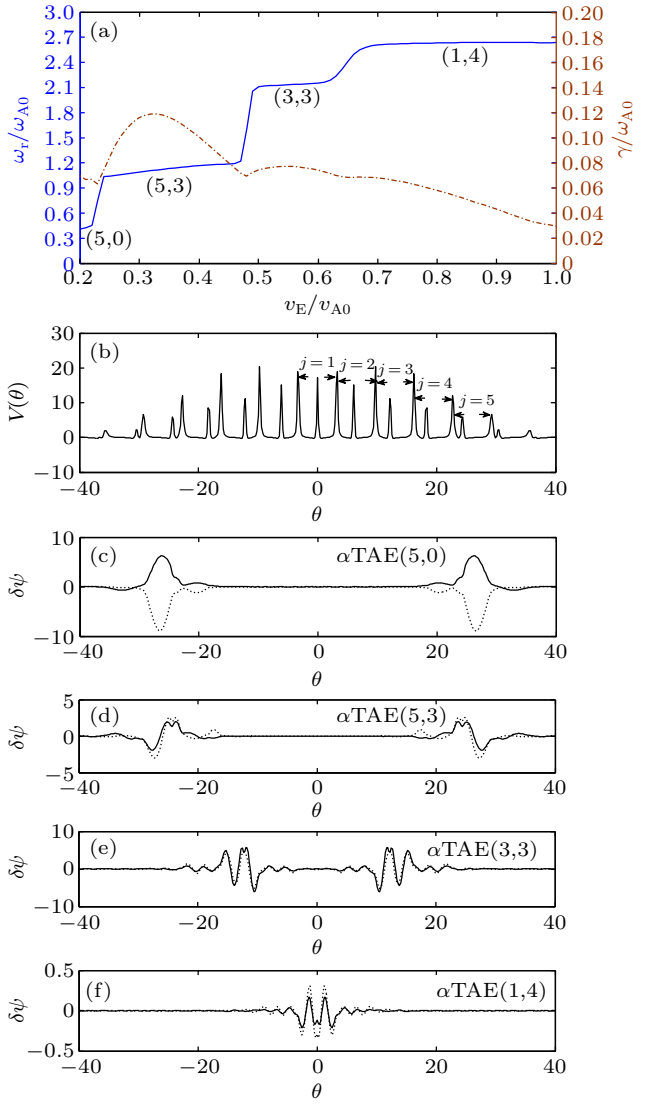


Fig. 3. (a) Real frequencies ω_r/ω_{A0} and growth rates γ/ω_{A0} versus v_E/v_{A0} for the [10°, 70°] condition at $\rho = 0.24$. (b) The potential well, (c) αTAE (5, 0), (d) αTAE (5, 3), (e) αTAE (3, 3) and (f) αTAE (1, 4) versus θ in the hybrid model; the solid and dashed lines are, respectively, the real and imaginary components.

growth rates are $\gamma/\omega_{A0} = 0.077$, 0.119, 0.077, and 0.066, respectively. Note that, with the increase in v_E/v_{A0}, the αTAE with higher real frequency ω_r/ω_{A0} can be excited.

In the range of [70°, 110°], the excitation of αTAEs versus v_E/v_{A0} is plotted in Fig. 4(a). As the v_E/v_{A0} increases, only the (5,3) mode is excited for $v_E/v_{A0} < 0.6$. The maximal growth rate of the (5,3) mode is 0.042. The (5,3) mode is excited in both the [10°, 70°] and the [70°, 110°] conditions. Compared with the (5,3) mode for [70°, 110°], the (5,3) mode for [10°, 70°] has a relatively large growth rate. It implies that the (5,3) mode is easier to excite in the range of [10°, 70°].

As a result, the simulation results indicate that one mode is excited at [70°, 110°] and four modes are excited at [10°, 70°], which implies that the αTAEs are easy to excite in the range of [10°, 70°].

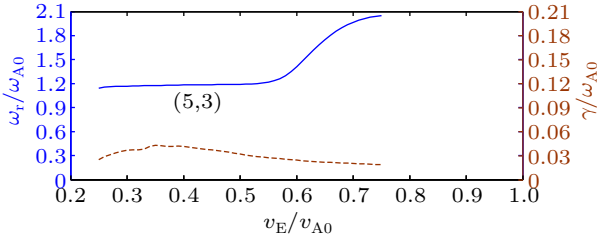


Fig. 4. Real frequencies ω_r/ω_{A0} and growth rates γ/ω_{A0} versus v_E/v_{A0} for the [70°, 110°] condition at $\rho = 0.24$.

3.3. αTAEs in the different EC power scenarios

We now investigate the αTAE stability in the different EC power scenarios. Based on the plasma profiles of Ref. [24], figures 5(a)–5(c) display the αTAE (1,0) mode distributions and figure 5(d) plots the s profiles of different EC power conditions. The EC power is 65 MW, 75 MW, and 112 MW, respectively.[24] The corresponding EC power deposition regions are as follows: $\rho \approx 0.45$–0.8; $\rho \approx 0.38$–0.6; $\rho \approx 0.3$–0.6.

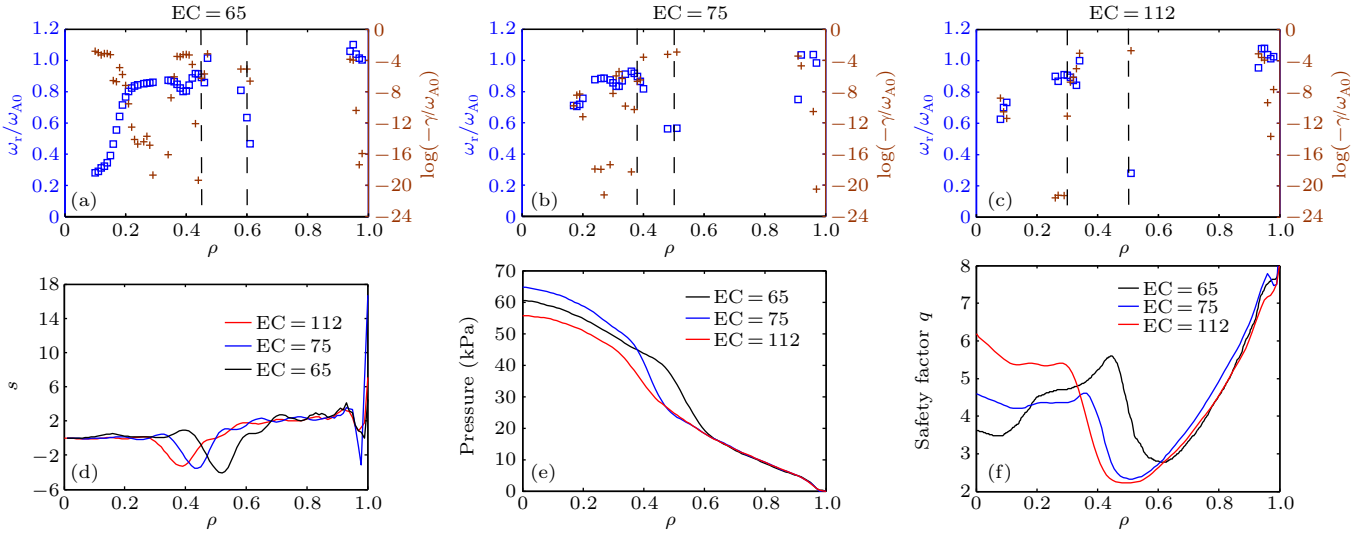


Fig. 5. (a)–(c) The distributions of αTAE (1,0) mode. (d) The parameter s profiles, (e) the pressure profiles[24] and (f) the q profiles[24] for different EC power conditions.

With the increasing EC power, the radial location of the ITB moves inward simultaneously with the EC-driven current profile.[24] Therefore, as shown in Figs. 5(a)–5(c) and 5(e), the pressure gradient is steep in the different EC power deposition regions, which forms the potential wells to trap the αTAEs. The αTAEs are trapped in the EC power deposition region, as shown in Figs. 5(a)–5(c). As shown in Fig. 5(d), the $|s|$ in the EC power deposition region becomes smaller with the increase in the EC power. Therefore, more αTAEs are trapped in the EC power deposition region with the increase in the EC power. With the increasing EC power, the temperature gradients in the inner core region are reduced.[24] Therefore, the greater the EC power in the EC power deposition region, the flatter the pressure gradient in the inner core region. Therefore, fewer αTAEs are located in the inner core region with the increase in EC power.

We conclude that, with the increase in the EC power, more αTAEs are trapped in the EC power deposition region and fewer αTAEs are trapped in the inner core region.

4. αTAEs in different pedestal case

Different pedestals have effects on the core plasma performance for different operation scenarios.[38] In Ref. [38], there are two different pedestal operation conditions; their pressure profiles and q profiles are different at the core or pedestal. Based on the two different pedestal operation conditions, we further explore the αTAE. These following pressure profiles and q profiles are quoted from Ref. [38]. Based on the plasma profiles, figures 6(a)–6(c) and 8(a)–8(c) display the αTAE (1,0) mode distributions for different cases. The pedestal region is in about $\rho \approx 0.9$–1.0.[38]

When the pedestal density is fixed, the higher pedestal temperature results in larger pedestal pressure gradients. The pedestal pressure gradients of three cases from small to large are as follows:[38] case 1, case 2, case 3. The pedestal pressure gradient becomes steeper, which forms potential wells to trap αTAEs. As shown in Figs. 6(a)–6(c) and 7(a), case 3 (the steepest pedestal pressure gradient) traps more αTAEs than the other two cases in the pedestal region. With the increase in the pedestal temperature, the pedestal moves inward from the plasma edge[38] and the pedestal width becomes wider; the αTAEs are bound in the wider region. For case 3, the ITB in $\rho \approx 0.4$–0.65 is weak;[38] therefore, the pressure gradient in $\rho \approx 0.4$–0.65 is flat, which does not trap the αTAEs, as shown in Figs. 6(c) and 7(a). The on-axis NBI produces a broad current profile.[38] Therefore, the αTAEs of the three cases are located in $\rho \approx 0$–0.4, as shown in Figs. 6(a)–6(c).

When the pedestal temperature is fixed, the higher pedestal density results in the larger pedestal pressure gradients. The pedestal pressure gradients of three cases from small to large are as follows:[38] case 4, case 5, and case 6. Similar to the fixed pedestal density cases, as the pedestal pressure gradient becomes steeper, there are more bound αTAEs in the pedestal region. As shown in Figs. 8 and 9(a), case 6 (the steepest pedestal pressure gradient) traps more αTAEs than the other two cases. With the increasing pedestal density, the

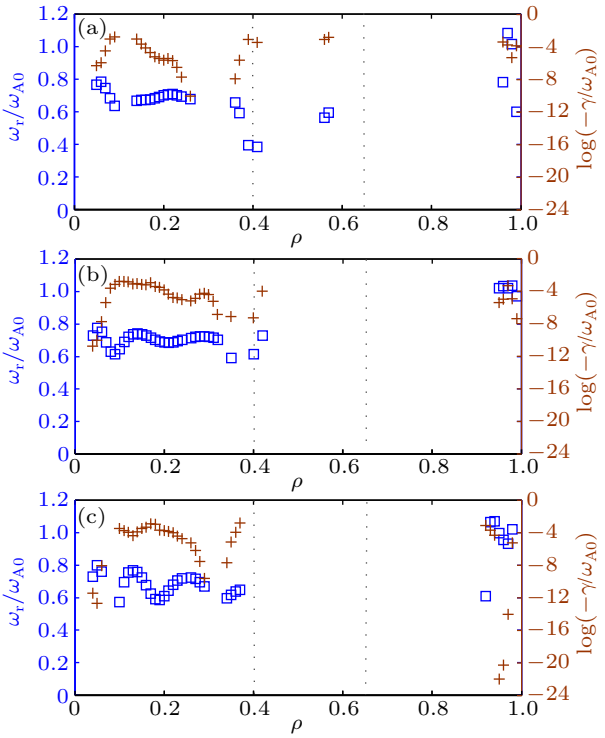


Fig. 6. (a) Case 1, (b) case 2, and (c) case 3 are the frequency profiles of the αTAE (1,0) mode, where the squares (□) and crosses (+) are, respectively, described as ω_r/ω_{A0} and $\log(-\gamma/\omega_{A0})$ versus ρ.

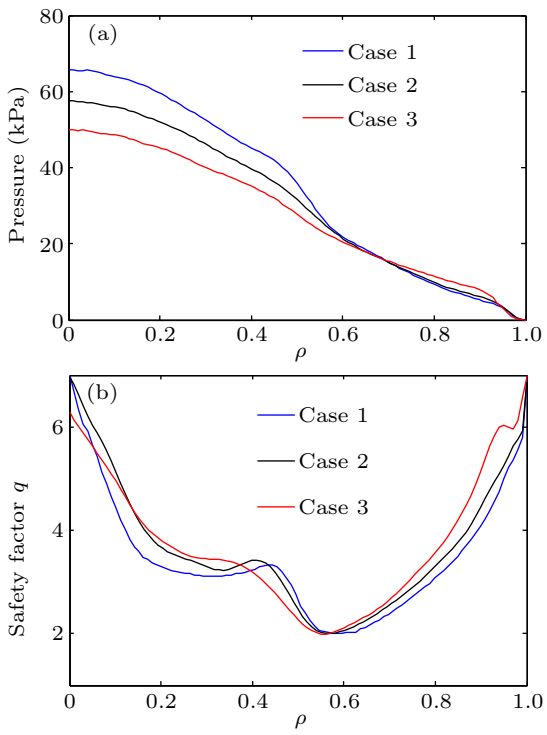


Fig. 7. (a) The pressure profiles and (b) the safety factor q profiles for three fixed pedestal density cases.

αTAEs are bound in the wider region. The fixed pedestal density cases operate with a moderate pedestal density to avoid giant edge-localized modes (ELMs).[38] Compared with the fixed pedestal temperature cases, relatively more αTAEs are trapped in the pedestal region of the fixed pedestal density cases, as shown in Figs. 6 and 8. The fixed pedestal density cases have relatively more impact on the stability of the αTAEs.

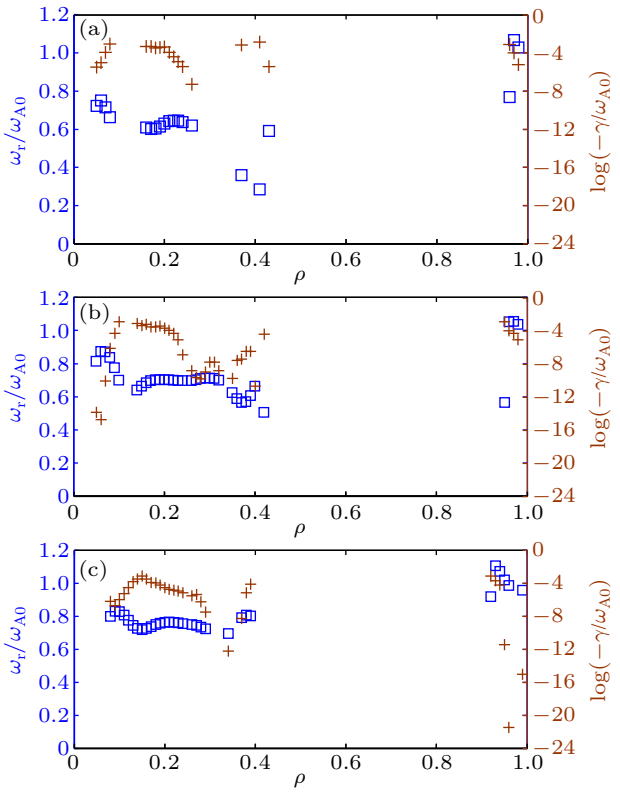


Fig. 8. (a) Case 4, (b) case 5, and (c) case 6 are the frequency profiles of the αTAE (1,0) mode, where the squares (□) and crosses (+) are, respectively, ω_r/ω_{A0} and $\log(-\gamma/\omega_{A0})$ versus ρ.

In the fixed pedestal density cases and the fixed pedestal temperature cases, the fusion power of both case 1 and case 6 is over 1 GW. With regard to case 1 and case 6, we explore the excitation of αTAEs versus v_E/v_{A0} in the different pitch-angle distributions. The different pitch-angle distributions are as follows: [10°, 70°] and [70°, 110°].

In case 1, we choose the local parameter with $\rho = 0.26$, $s = -0.1$, $\alpha = 3.14$, $q = 2.19$; the remaining parameters are the same as in Fig. 3. For case 1, [10°, 70°], figure 10(a) plots the real frequency and growth rate as functions of v_E/v_{A0}. As the v_E/v_{A0} increases, the three eigenmodes (1,0), (4,2), and (1,2) are excited. Figures 10(c)–10(e) show the eigenmode structures of $v_E/v_{A0} = 0.28$, 0.42, and 0.65, respectively. The real frequencies of the three modes are $\omega_r/\omega_{A0} = 0.45$, 0.91, and 1.54, respectively. Their growth rates are $\gamma/\omega_{A0} = 0.170$, 0.140, and 0.104, respectively. Therefore, the (1,0) mode is the most unstable mode in the three modes in terms of the growth rate.

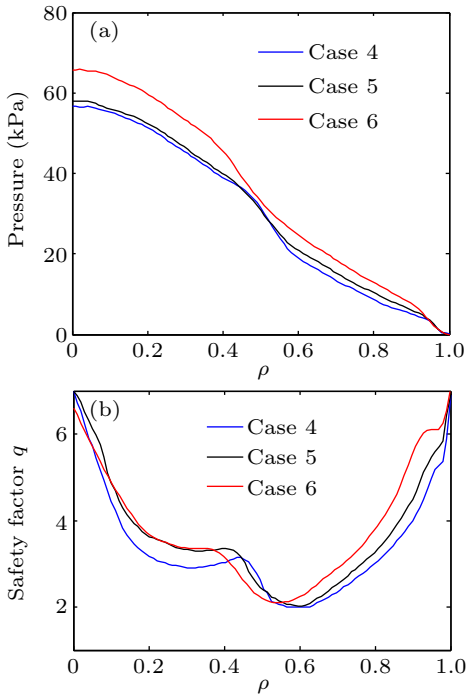


Fig. 9. (a) The pressure profiles and (b) the safety factor q profiles for three fixed pedestal temperature cases.

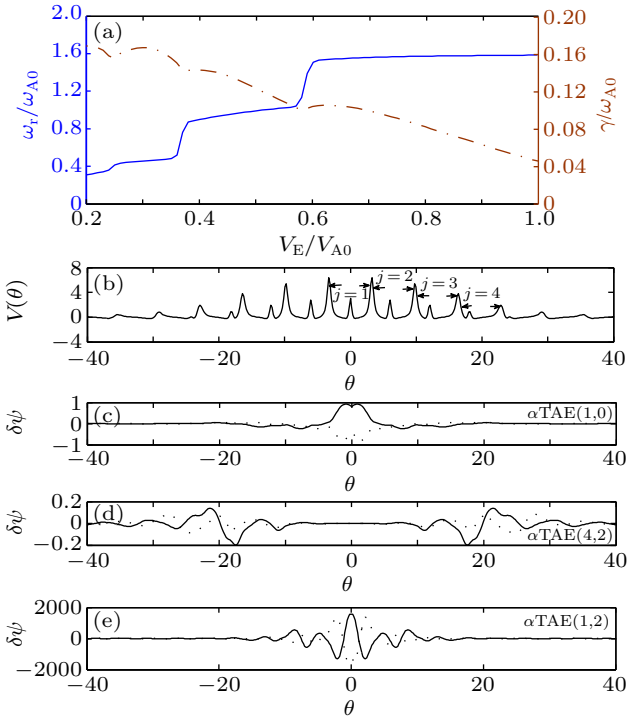


Fig. 10. (a) The real frequencies ω_r/ω_{A0} and growth rates γ/ω_{A0} versus v_E/v_{A0} in the range of [10°, 70°] for case 1. (b) The potential well, (c) αTAE (1, 0), (d) αTAE (4, 2), and (e) αTAE (1, 2) versus θ in the hybrid model; the solid and dashed lines are, respectively, the real and imaginary components.

For case 1, [70°, 110°], figure 11(a) plots the real frequency and growth rate as functions of v_E/v_{A0}. There are two modes to be excited, which are less than case 1 for the range of [10°, 70°]. Figures 11(c) and 11(d) show the eigenmode structures of $v_E/v_{A0} = 0.20$ and 0.45, respectively. The real frequencies of the two modes are $\omega_r/\omega_{A0} = 0.30$ and 0.88, re-

spectively. Their growth rates are $\gamma/\omega_{A0} = 0.108$ and 0.115, respectively.

In case 6, we choose the local parameter with $\rho = 0.29$, $s = -0.16$, $\alpha = 2.45$, $q = 3.46$; the remaining parameters are the same as in Fig. 3. There are three modes that are excited in both the [10°, 70°] and the [70°, 110°] conditions, as shown in Figs. 12(a) and 12(b). Therefore, compared with case 6, the [70°, 110°] conditions of case 1 have less impact on the stability of the αTAEs.

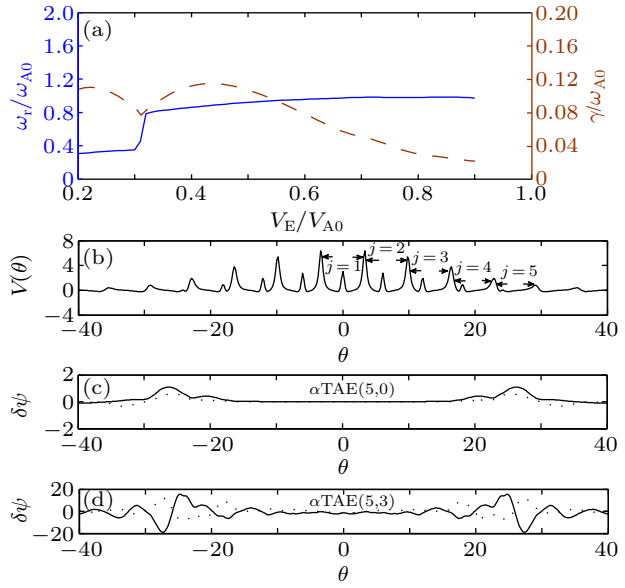


Fig. 11. (a) The real frequencies ω_r/ω_{A0} and growth rates γ/ω_{A0} versus v_E/v_{A0} in the range of [70°, 110°] for case 1. (b) The potential well, (c) αTAE (5, 0), and (d) αTAE (5, 3) versus θ in the hybrid model; the solid and dashed lines are, respectively, the real and imaginary components.

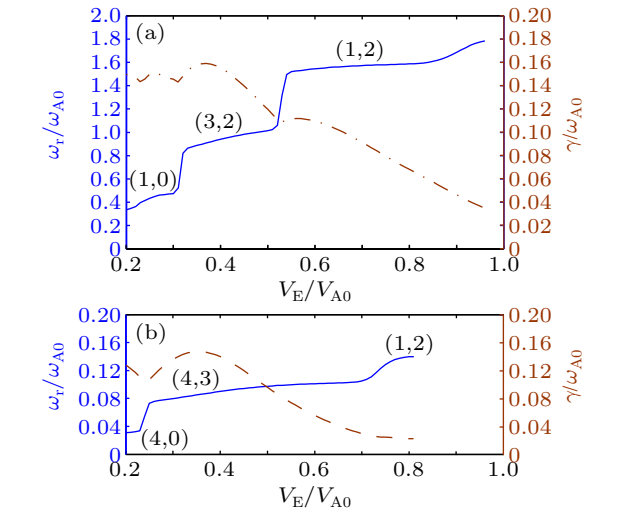


Fig. 12. (a) The real frequencies ω_r/ω_{A0} and growth rates γ/ω_{A0} versus v_E/v_{A0} in the range of [70°, 110°] for case 6. (b) The real frequencies ω_r/ω_{A0} and growth rates γ/ω_{A0} versus v_E/v_{A0} in the range of [70°, 110°] for case 6.

So far, we have studied the stability of αTAEs in the different pedestal cases. The key finding is that more αTAEs are trapped in the wider pedestal region with the increase in the pedestal pressure gradient. Compared with the fixed pedestal temperature cases, relatively more αTAEs are trapped in the pedestal region of the fixed pedestal density cases. This demonstrates that the fixed pedestal density cases have more effects on the αTAEs. In the different pitch-angle distributions of case 1 and case 6, multiple branches of αTAEs are excited. Compared with case 6, fewer branches of αTAEs are excited in the [70°, 110°] conditions of case 1. This implies that the [70°, 110°] conditions of case 1 have less impact on the stability of the αTAEs.

5. αTAEs in the negative off-axis magnetic shear scenario

The negative off-axis magnetic shear is considered as a possible solution to the steady-state scheme, in which an improved-confinement internal transport barrier (ITB) can be sustained at a far off-axis location, and the fusion power of the entire plasma can be increased.[39] We discuss the instability of αTAEs in different negative magnetic shear locations. The following pressure profiles and q profiles in three cases are quoted from Refs. [26,39,40], respectively. Based on the plasma profiles, the αTAE (1,0) mode distributions of the three cases are displayed in Figs. 13(a) and 14(a).

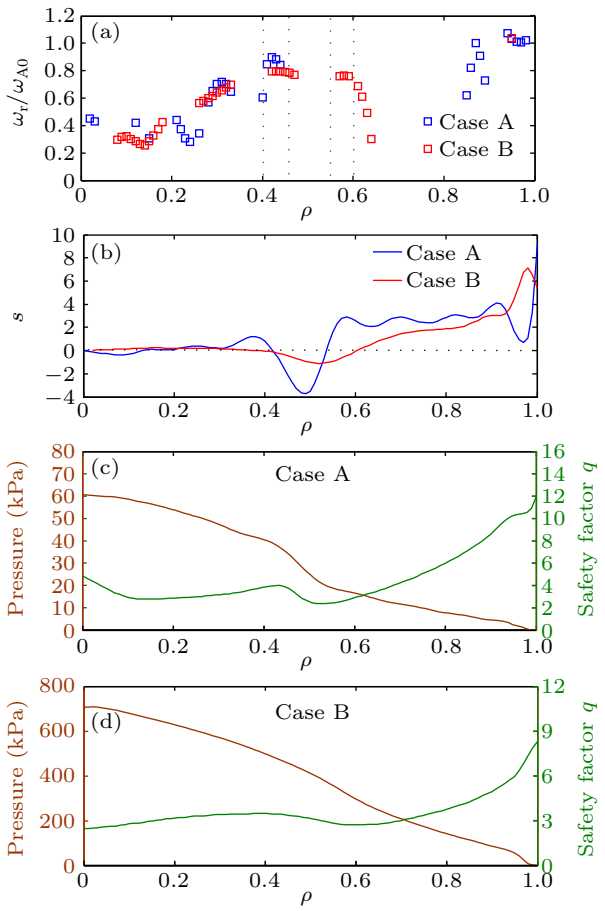


Fig. 13. (a) The real frequency ω_r/ω_{A0} profile of αTAE (1, 0) in two negative off-axis magnetic shears. (b) The parameter s of the two cases versus ρ. (c) The pressure profile and the q profile in case A.[26] (d) The pressure profile and the q profile in case B.[39]

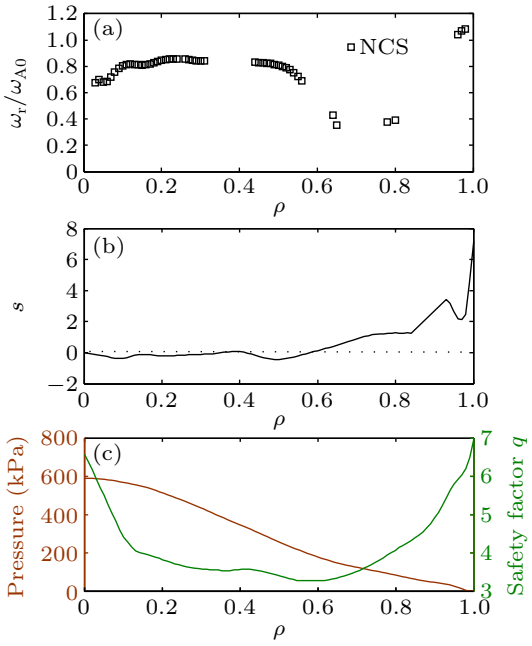


Fig. 14. (a) The real frequency ω_r/ω_{A0} profile of αTAE (1, 0) in the NCS. (b) The parameter s of the NCS versus ρ. (c) The pressure profile and the q profile in the NCS.[40]

5.1. The effect of the negative shear location on αTAEs

We first explore the αTAE in the negative off-axis magnetic shears. For the region of $\rho \approx 0.45$–0.55[26] (case A), the negative magnetic shear region, there is a major bootstrap current and the ECCD.[26] As shown in Figs. 13(a)–13(c), the pressure gradient is steep but the $|s|$ is large in the negative magnetic shear region, which does not trap the αTAEs. The $J = -\overline{V}\sqrt{\frac{r}{R}}\frac{1}{B_\theta}\frac{\mathrm{d}p}{\mathrm{d}r}$ [41] is obtained by the bootstrap current model[42] ($\overline{V}$: the particle collision parameter, B_θ: the poloidal magnetic, p: plasma pressure). Therefore, the αTAEs are located in $\rho \approx 0.9$–1.0 because there is a minor bootstrap current peak. In the $\rho \approx 0.5$–0.8 region, the positive magnetic shear value is large and the pressure gradient is not steep enough, which is the unstable region of the ballooning mode. The αTAEs are not trapped in the $\rho \approx 0.5$–0.8 region.

As a reference, the αTAE of the negative magnetic shear region[39] (case B) is explored. In the $\rho \approx 0.4$–0.6 region, there is the superposition of the low hybrid current drive (LHCD) and the ECCD at $\rho \approx 0.55$.[39] Therefore, the αTAEs are located in the $\rho \approx 0.4$–0.6 region because the $|s|$ is relatively small, as shown in Figs. 13(a), 13(b) and 13(d).

For comparison with the negative off-axis magnetic shears, we then explore the αTAE in the negative central shear (NCS).[40] In the $\rho \approx 0$–0.6 region, the negative magnetic shear region, there is a broad bootstrap current and the ECCD deposited in the $\rho \approx 0.2$ and the $\rho \approx 0.4$–0.8 regions.[40] As shown in Figs. 14(a)–14(c), the broad $|s|$ is small and the pressure gradient is steep. Therefore, the αTAEs are located in the negative magnetic shear region.

The distributions of αTAE (1,0) mode demonstrate that many αTAEs are trapped in the three different negative magnetic shear cases. However, we find that the αTAEs in the NCS are trapped more than the negative off-axis magnetic shear. This is because of the broad small $|s|$ and the steep pressure gradient in the NCS. The αTAEs of case B are trapped more than case A in the negative magnetic shear region. This is because the $|s|$ is large.

5.2. The effect of the beam energies on αTAE stability

The different beam energies are chosen according to the different cases. The injected energetic particles bring a wide velocity distribution in the process of slowing down. The particle's velocity will affect the curvature drift frequency; therefore, different velocities will affect the excitation of the branches of the αTAEs. We investigate the effect of different beam energies on the αTAE stability. For case B, the negative off-axis shear ($\rho \approx 0.4$–0.6), the energetic particle energies introduced by NBI are about 150 keV and 400 keV in Ref. [39], in which the corresponding v_E/v_{A0} is 0.40 and 0.66, respectively. For the NCS ($\rho \approx 0$–0.6), the energetic particle energies introduced by NBI are about 100 keV and 500 keV in Ref. [40], in which the corresponding v_E/v_{A0} is 0.35 and 0.77, respectively. The local parameter with $s = -0.15$, $\alpha = 3.14$, $q = 3.44$ is in case B; the local parameter with $s = -0.11$, $\alpha = 3.35$, $q = 3.96$ is in the NCS; the remaining parameters of the two cases are the same as in Fig. 3.

In case B, the excitation of αTAEs versus v_E/v_{A0} is plotted in Fig. 15(a). As shown in Fig. 15(a), the (4,0) mode and the (4,3) mode are excited and become unstable modes when $v_E/v_{A0} < 0.40$; meanwhile, the (4,0) mode, (4,3) mode and (1,2) mode are excited and become unstable modes when $v_E/v_{A0} < 0.66$, in which ω_r/ω_{A0} is 0.39, 1.04, and 1.60, respectively. The (1,4) mode is not excited by the energetic particles introduced by case B. When we consider the higher energetic particles, the (1,4) mode will be excited, in which ω_r/ω_{A0} is 2.53. In the NCS, the excitation of αTAEs versus v_E/v_{A0} is plotted in Fig. 15(b). As shown in Fig. 15(b), the (5,3) mode is excited and becomes the unstable mode when $v_E/v_{A0} < 0.35$; meanwhile, the (5,3) mode and (1,2) mode are excited and become unstable modes when $v_E/v_{A0} < 0.77$, in which ω_r/ω_{A0} is 1.08 and 1.61, respectively. The (3,3) mode is not excited until the higher energetic particles introduced by the NCS, in which ω_r/ω_{A0} is 2.10.

Three modes are excited and become the unstable modes in case B, while two modes are excited and become the unstable modes in the NCS, which implies that the energetic particles in case B have more impact on the stability of the αTAEs. In case B and the NCS, the energetic particles with higher energy find it easier to destabilize the higher real frequency of the αTAEs.

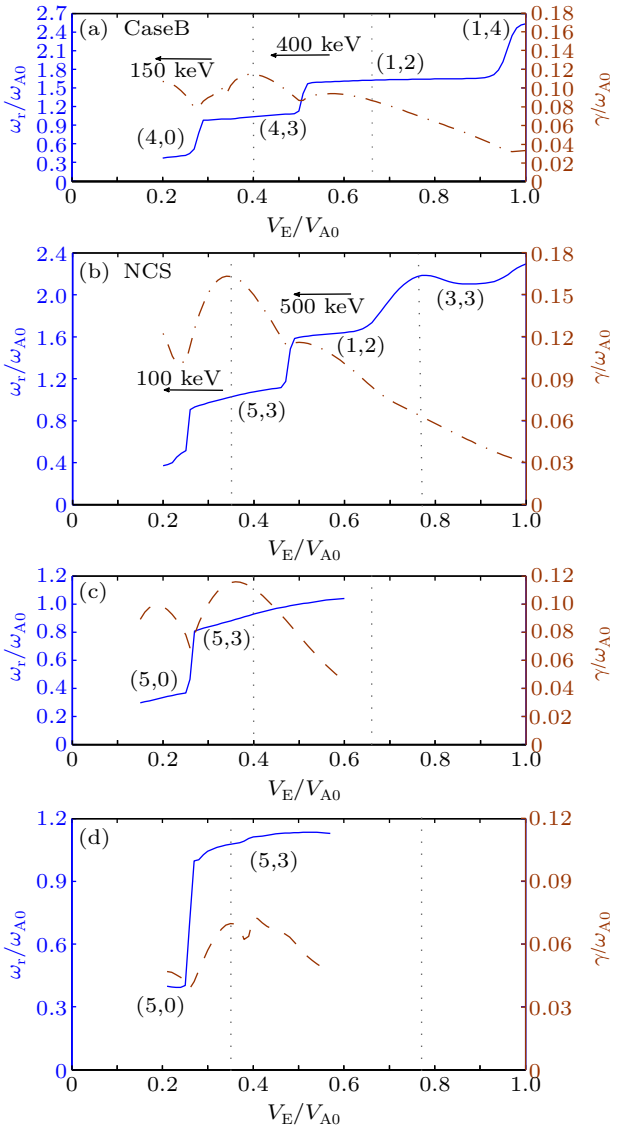


Fig. 15. The real frequencies ω_r/ω_{A0} and growth rates γ/ω_{A0} versus v_E/v_{A0} in the [10°, 70°] condition in (a) case B and (b) the NCS; the real frequencies ω_r/ω_{A0} and growth rates γ/ω_{A0} versus v_E/v_{A0} in the [70°, 110°] condition in (c) case B and the (d) NCS.

5.3. The effect of the pitch-angle distributions on αTAE stability

For case B and the NCS, we explore the excitation of αTAEs versus v_E/v_{A0} in the different pitch-angle distributions. Figures 15(a) and 15(b) plot the [10°, 70°] conditions of case B and the NCS, respectively. Figures 15(c) and 15(d) plot the [70°, 110°] conditions of case B and the NCS, respectively.

As shown in Fig. 15(c), the (5,0) mode and the (5,3) mode are excited by energetic particles in case B, in which ω_r/ω_{A0} is 0.29 and 0.92, respectively. As shown in Fig. 15(d), the (5,0) mode and the (5,3) mode are excited by energetic particles in the NCS, in which ω_r/ω_{A0} is 0.39 and 1.04, respectively.

In case B and the NCS, there are different αTAEs that are excited in the different pitch-angle distributions. For case B, there are fewer unstable modes in the range of [70°, 110°], as shown in Figs. 15(a)–15(c). For the NCS, there are lower frequency unstable modes in the range of [70°, 110°], as shown in Figs. 15(b)–15(d); the maximal growth rate γ/ω_{A0} of the (5,3) mode in the range of [10°, 70°] is 0.163, while the maximal growth rate γ/ω_{A0} of the (5,3) mode in the range of [70°, 110°] is 0.069, which shows that the (5,3) mode in the range of [10°, 70°] is easier to excite. In summary, these results indicate that the αTAEs are easy to excite in the [10°, 70°] conditions of case B and the NCS. The [10°, 70°] conditions of case B and the NCS have more impact on the αTAE stability.

6. Conclusion

In this paper, αTAE stability is investigated using the gyrokinetic-MHD hybrid model in the CFETR advanced steady-state operation environment, which includes the RS H-mode scenario with an enhanced ITB and the negative off-axis magnetic shear scenario. In the RS H-mode scenario with the enhanced ITB, the αTAEs are located in the EC power deposition region. As the pedestal density or the pedestal temperature increases, the pedestal pressure gradient becomes steep, and more αTAEs are trapped in the pedestal region.

We discuss αTAEs in the negative off-axis magnetic shear scenario. In the $\rho \approx 0.45$–0.55 region (case A), there is a bootstrap current and the ECCD. In the $\rho \approx 0.4$–0.6 region (case B), there is the superposition of the LHCD and the ECCD at $\rho \approx 0.55$. In the negative magnetic shear region, the αTAEs are trapped in case B rather than case A because the $|s|$ of case B is small. For comparison with the negative off-axis magnetic shear, we explore the αTAEs in the NCS. There are many αTAEs that become trapped in the negative magnetic shear region because of the broad small $|s|$ and the steep pressure gradient.

With the variation of beam energy and pitch-angle distributions, multiple branches of αTAEs are excited in the presence of energetic particles. Further results reveal that the energetic particles with higher energy find it easier to destabilize the higher real frequency αTAEs. The αTAEs are easy to excite in the large pitch-angle distribution.

The Alfvén instabilities driven by alpha particles are a concern for future tokamak devices. We will further explore the excitation of αTAEs by alpha particles in the CFETR.

Acknowledgment

Project supported by the National Natural Science Foundation of China (Grant Nos. 11775058 and 12175049).

References

[1] Wan Y X, Li J G, Liu Y, *et al.* 2017 *Nucl. Fusion* **57** 102009
[2] Wan B N, Ding S Y, Qian J P, Li G Q, Xiao B J and Xu G S 2014 *IEEE Trans. Plasma Sci.* **42** 495
[3] Neilson G H, Federici G, Li J, Maisonnier D and Wolf R 2012 *Nucl. Fusion* **52** 047001

[4] Zohm H, Angioni C, Fable E, Federici G, Gantenbein G, Hartmann T, Lackner K, Poli E, Porte L, Sauter O, Tardini G, Ward D and Wischmeier M 2013 *Nucl. Fusion* **53** 073019

[5] Zou Y P and Ye M Y 2019 *Plasma Sci. Technol.* **21** 095104

[6] Yang W J, Li G Q, Gong X Y, Gao X and Li X E 2021 *Plasma Sci. Technol.* **23** 045103

[7] Ren Z Z, Chen Y, Fu G Y and Wang Z X 2020 *Nucl. Fusion* **60** 016009

[8] Varela J, Huang J, Spong D A, Chen J, Chan V, Garcia L, Wingen A, Ghai Y and Zou Y 2022 *Nucl. Fusion* **62** 036005

[9] Cheng C Z, Chen L and Chance M S 1985 *Ann. Phys.* **161** 21

[10] Yang W J, Li G Q, Hu Y J and Gao X 2017 *Fusion Eng. Des.* **114** 118

[11] Zhu X L, Wang F and Wang Z X 2020 *Chin. Phys. B* **29** 025201

[12] Chen W, Yu L M, Liu Y, *et al.* 2014 *Nucl. Fusion* **54** 104002

[13] Zhang T, Liu H Q, Li G Q, Zeng L, Yang Y, Ming T F, Gao X, Lian H, Li K, Liu Y, Li Y Y, Shi T H, Han X and the EAST team 2018 *Plasma Sci. Technol.* **20** 115101

[14] Wang W J, Zhou D, Hu Y J, *et al.* 2018 *Chin. Phys. B* **27** 125202

[15] Hu S and Chen L 2004 *Phys. Plasmas* **11** 1

[16] Hu S and Chen L 2005 *Plasma Phys. Control. Fusion* **47** 1251

[17] Wang J, Hu C D, Hu S S, Wu B and Ding S Y 2013 *Plasma Sci. Technol.* **15** 750

[18] Wang J, Hu S S, Dai Q P and Yao L B 2010 *Chin. Phys. B* **19** 095202

[19] Wu H, Hu S S, He Q M, Zhao Z L and Jiang L 2018 *J. Fusion Energy* **37** 238

[20] Wang J, Hu C D, Hu S S, Wu B, Ding S Y and Wang J F 2013 *Acta Phys. Sin.* **62** 035201 (in Chinese)

[21] Wang Y R, Hu S S, Yao L B and Chen S P 2012 *Nucl. Fusion Plasma Phys.* **32** 140 (in Chinese)

[22] Zhao Q F, Hu S S, He Q M and Ou-Yang X F 2020 *Sci. Sin-Phys. Mech. Astron.* **50** 085211 (in Chinese)

[23] Zou Y P, Chan Vincent S, Huang J, Collins C S, Garofalo A M, Guo W F and Ye M Y 2019 *Nucl. Fusion* **59** 066005

[24] Zhou C X, Chen J L, Chan Vincent, Jian X and Zhuang G 2022 *Phys. Plasmas* **29** 022505

[25] Garcia J, Giruzzi G, Artaud J F, Basiuk V, Decker J, Imbeaux F, Peysson Y and Schneider M 2008 *Plasma Phy. Control. Fusion* **50** 124032

[26] Qian J P, Garofalo A M, Gong X Z, *et al.* 2021 *Phys. Plasmas* **28** 042506

[27] Connor J W, Hastie R J and Taylor J B 1979 *Proc. R. Soc. Lond. A* **365** 1

[28] Connor J W, Hastie R J and Taylor J B 1978 *Phys. Rev. Lett* **40** 396

[29] Chen L 1994 *Phys. Plasmas* **1** 1519

[30] Chen L and Hasegawa A 1991 *Journal of Geophysical Research: Space Physics* **96** 1503

[31] Parker S E and Lee W W 1993 *Phys. Fluids B* **5** 77

[32] Dettrick S, Zheng L J and Chen L 2003 *J. Geophys. Res.* **108** 5

[33] Birdsall C K and Langdon A B 1985 *Plasma Physics via Computer Simulation* (New York: McGraw-Hill) pp. 55–60

[34] Zheng L J, Chen L and Santoro R A 2000 *Phys. Plasmas* **7** 2469

[35] Li J Q and Shi B R 1992 *Nucl. Fusion Plasma Phys.* **12** 233 (in Chinese)

[36] Santoro R A and Chen L 1996 *Phys. Plasmas* **3** 2349

[37] Huang Q H 2015 *Heating of plasma and bootstrap current of fast ions in neutral beam injection* (Ph.D.dissertation) (Hengyang: University of South China) (in Chinese)

[38] Zhou C X, Chen J L, Chan V S, Jian X, Zhuang G, Zhu Y R and CFETR team 2020 *Nucl. Fusion* **60** 096029

[39] Zhong Y J, Huang Q H, Gong X Y, Tan Q Y, Zheng P W, Wang J and Shi Y F 2021 *Fusion Eng. Des.* **172** 112912

[40] Zhuang G, Li G Q, Li J, Wan Y X, Liu Y, Wang X L, Song Y T, Chan V, Yang Q W, Wan B N, Duan X R, Fu P, Xiao B J and the CFETR Design Team 2019 *Nucl. Fusion* **59** 112010

[41] Bickerton R J, Connor J W and Taylor J B 1971 *Nat. Phys. Sci.* **229** 110

[42] Li H, Wu B, Wang J, *et al.* 2015 *Plasma Sci. Technol.* **17** 10